The Astrophysical Journal, 856:159 (16pp), 2018 April 1 https://doi.org/10.3847/1538-4357/aab495

A Tractable Estimate for the Dissipation Range Onset Wavenumber Throughout the Heliosphere

N. Eugene Engelbrecht[1,2] and R. Du Toit Strauss[1,2]
[1] Center for Space Research, North-West University, Potchefstroom, 2522, South Africa; n.eugene.engelbrecht@gmail.com
[2] National Institute for Theoretical Physics (NITheP), Gauteng, South Africa
Received 2018 January 9; revised 2018 February 12; accepted 2018 March 2; published 2018 April 4

Abstract

The modulation of low-energy electrons in the heliosphere is extremely sensitive to the behavior of the dissipation range slab turbulence. The present study derives approximate expressions for the wavenumber at which the dissipation range on the slab turbulence power spectrum commences, by assuming that this onset occurs when dispersive waves propagating parallel to the background magnetic field gyroresonate with thermal plasma particles. This assumption yields results in reasonable agreement with existing spacecraft observations. These expressions are functions of the solar wind proton and electron temperatures, which are here modeled throughout the region where the solar wind is supersonic using a two-component turbulence transport model. The results so acquired are compared with extrapolations of existing models for the dissipation range onset wavenumber, and conclusions are drawn therefrom.

Key words: solar wind – Sun: heliosphere – turbulence – waves

1. Introduction

To model the transport of low-energy cosmic-ray electrons, we need information about the dissipation range of the slab spectrum as it has turbulent fluctuations at such scales where low-energy electrons resonate and are pitch-angle-scattered parallel to the mean field (see, e.g., Bieber et al. 1994; Engelbrecht & Burger 2013b; Strauss et al. 2017). This has indeed been demonstrated by Engelbrecht & Burger (2010), who showed, by employing electron parallel mean free path expressions constructed in the appropriate limits from expressions derived from quasi-linear theory (QLT; see, e.g., Jokipii 1966) by Teufel & Schlickeiser (2003), that galactic cosmic-ray electron intensities computed using a 3D modulation code are extremely sensitive to choices made for quantities pertinent to the dissipation range of the slab turbulence power spectrum, such as its spectral index and the wavenumber k_d at which this range commences, a result confirmed by Engelbrecht & Burger (2013b). It would therefore be important to a greater understanding of the transport of these low-energy electrons to find a tractable, implementable estimate for the wavenumber where the onset of the turbulence dissipation range occurs. Previous work by Leamon et al. (2000) does indeed provide fits to observations of this quantity at Earth, which were employed by Engelbrecht & Burger (2010, 2013b) to model this quantity, but it is uncertain whether extrapolations of fits to data taken at 1 au would provide a reasonable estimate for k_d throughout the heliosphere. The present study aims to provide an alternative means of estimating k_d that would provide tractable estimates that could readily be employed in the study of the transport of galactic, as well as Jovian, electrons. We assume here that the slab component of the anisotropically turbulent solar wind is dominant in the dissipation range, an assumption motivated by spacecraft observations at 1 au (see the review by Oughton et al. 2015 and references therein). Moreover, we assume that the slab component of the turbulence consists of dispersive parallel propagating wave modes and that gyroresonance with thermal plasma particles (evidence for which have been reported by Roberts & Li 2015) damp the wavelike spectrum, leading to the dissipation range, while heating the plasma. The idea of cyclotron damping of the slab component is not new (e.g., Coleman 1968) and has in the past been used to explain the observed onset of the dissipation range (e.g., Leamon et al. 1998a, 1998b). Currently, it remains the preferred process to explain the dissipation of slab fluctuation energy (see, e.g., Smith et al. 2012). We derive tractable expressions for k_d and show that these depend on the magnetic polarity of the waves that are considered. A further result is that, when a composite slab spectrum is constructed, a second inertial range is present, containing an enhancement of right-hand polarized Whistler modes.

The second part of this study calculates k_d by modeling the solar wind proton and electron temperatures using a turbulence transport model (TTM) that incorporates the effects of wave generation due to pickup-ion formation in the outer heliosphere (see, e.g., Zank 1999; Isenberg 2005; Cannon et al. 2014; Aggarwal et al. 2016; Hellinger & Trávníček 2016). Although this has been attempted before for both species (see Breech et al. 2009), most studies of this kind focus only on the solar wind proton temperature (see, e.g., Ng et al. 1998; Smith et al. 2001; Breech et al. 2008; Isenberg et al. 2010), employing single-component turbulence transport models. To model the solar wind proton and electron temperatures, we apply an approach similar to that taken by Breech et al. (2009), but, instead of using the single-component Breech et al. (2008) TTM, we instead use the two-component TTM proposed by Oughton et al. (2011), which describes the radial evolution of both Quasi-2D and wavelike turbulence quantities (see, e.g., Oughton et al. 2006) and thus provides for a more self-consistent treatment of the spatial variation of anisotropic turbulence quantities in the heliosphere. The use of the Oughton et al. (2011) model is largely motivated by the fact that energy due to various turbulent driving processes can be assigned to an appropriate component, as is the case with driving due to the formation of pickup ions (see, e.g., Hunana & Zank 2010). Although more advanced two-component turbulence transport models exist (see Wiengarten et al. 2016; Adhikari et al. 2017; Zank et al. 2017), we employ the

Oughton et al. (2011) model, motivated by its relative simplicity, and the fact that it yields results identical to those of the Wiengarten et al. (2016) model in the supersonic solar wind, which is the region of interest in this study. It can also yield results in agreement with spacecraft observations along the trajectory of the *Ulysses* spacecraft (Engelbrecht & Burger 2013a) and has been used before in galactic cosmic-ray electron modulation studies (Engelbrecht & Burger 2013b). The results from this approach are compared with existing turbulence data sets, as well as observations of the proton and electron temperatures in the ecliptic plane. We go on to compare the model results with temperatures observed by *Ulysses*, making our comparison along the actual trajectory of the spacecraft, which traverses a broad range of latitudes. Such a comparison has only before been done by Engelbrecht & Burger (2013a) for solar wind proton temperatures. Other studies of this kind usually compare model outputs along a radial "spoke" at a constant colatitude with *Ulysses* observations. Thereafter, we employ the TTM model temperature outputs to calculate estimates for k_d throughout the region of the heliosphere dominated by the supersonic solar wind. These estimates are then compared to extrapolations throughout the heliosphere of model fits to *Wind* observations reported by Leamon et al. (2000), as employed in cosmic-ray electron modulation studies by Engelbrecht & Burger (2010).

2. Dispersive Waves

The slab, or wavelike, turbulence component is assumed to consist of four waves,

$$W = \sum_{j=\pm 1} \omega^j_{\rm LH} + \sum_{j=\pm 1} \omega^j_{\rm RH}, \tag{1}$$

where we add waves propagating either forwards ($j = +1$) or backwards ($j = -1$) along the mean field, having either a left-handed (LH) or right-handed (RH) circular polarization mode. For now, we ignore any oblique propagation modes.

We start by using the dispersion relationships for the LH and RH circularly polarized waves in a cold plasma. This initial assumption implies zero temperature for both protons and electrons, $T_{\rm e} = T_{\rm p} = 0$, the implication of which will be further discussed later. The standard dispersion relations are given by (e.g., Stix 1962)

$$k^2_{\parallel,\rm LH} \approx \frac{\omega^2}{V^2_{\rm A}} \left\{ \frac{\Omega_p}{\Omega_p - \omega} \right\} \tag{2}$$

and

$$k^2_{\parallel,\rm RH} \approx \frac{\omega^2}{c^2} \left\{ \frac{|\Omega_e|}{|\Omega_e| - \omega} + \frac{\omega^2_e}{(|\Omega_e| - \omega)(\Omega_p + \omega)} \right\}, \tag{3}$$

where $k_\parallel$ is the parallel wavenumber, ω the frequency in the bulk (flow) plasma frame, c the speed of light, and $V_{\rm A}$ the Alfvén speed. Ω_p and $|\Omega_e|$ are the proton and electron cyclotron frequencies, given as

$$|\Omega_e| = \frac{|e|B}{m_e} = \Lambda \Omega_p, \tag{4}$$

where $\Lambda = m_p/m_e$ is the ratio between proton and electron masses, e the elementary charge, and B the mean background magnetic field, while the different plasma frequencies are given as

$$\omega_e = \sqrt{\frac{n_e e^2}{m_e \epsilon_0}} = \omega_p \sqrt{\Lambda}, \tag{5}$$

with n_e the electron number density and ϵ_0 the permittivity of free space. Note that we assume quasi-neutrality with $n_e \approx n_p$. In terms of these frequencies, $V_{\rm A}$ is

$$V_{\rm A} = c \frac{\Omega_p}{\omega_p}. \tag{6}$$

In deriving Equations (2) and (3), it was assumed that $\omega \ll \omega_p \ll \omega_e$ (see, e.g., Stix 1962).

Assuming solar wind conditions at 1 au, the dispersion relations are shown in Figure 1, while Table 1 lists the plasma quantities that were adopted and resulted from the calculations. The well-known behavior of dispersive, parallel propagating, circularly polarized waves is evident: for LH polarized waves (left panel), at low frequencies where $\omega \ll \Omega_p$, the LH mode reduces to the non-dispersive Alfvén mode, given by

$$\omega_{\rm A} = V_{\rm A} k_\parallel, \tag{7}$$

which is shown as the black dashed line. As $\omega \to \Omega_p$, the LH mode starts to be damped by a cyclotron resonance (see the next section), forming the proton-cyclotron branch. It is this part of the dispersion diagram that will be modified when we relax the assumption of $T_p = 0$, the effect of which is discussed later on.

For the RH model (right panel of Figure 1), we again reduce to the Alfvén branch when $\omega \ll \Omega_p$. Between $\Omega_p \ll \omega \ll |\Omega_e|$, we, however, find the Whistler branch,

$$\omega_W = c^2 k_\parallel^2 \frac{|\Omega_e|}{\omega^2_e}, \tag{8}$$

which is indicated on the figure by the green dashed line. A similar electron cyclotron mode is present as $\omega \to |\Omega_e|$.

3. Wave–Particle Interactions

In order for charged particles to gyroresonate with circularly polarized waves, we require, in the idealized case, that they have the same angular frequency in the particle's guiding center frame,

$$\boldsymbol{\omega}^* = \frac{d\boldsymbol{\varphi}}{dt} = -\boldsymbol{\Omega}^* \Rightarrow \mp \omega^* = -\Omega^*, \tag{9}$$

where ω^* and Ω^* are the wave and particle frequencies in the guiding center frame and φ the gyrophase. The equation states that the magnitude of the wave and particle frequencies should match, as well as their sense of rotation, hence the introduction of the $\mp$ sign, keeping $\omega^* \geqslant 0$. We introduce the integer $n = \pm 1$ to define the polarization of the wave, i.e., $n = +1$ for LH and $n = -1$ for RH polarized waves, so that Equation (9) becomes

$$\omega^* = n\Omega^*. \tag{10}$$

We can now transform back to the bulk flow frame (noting that the dispersion relations are given in this reference frame), by Doppler-shifting the frequencies by the particle velocity $\boldsymbol{v}$,

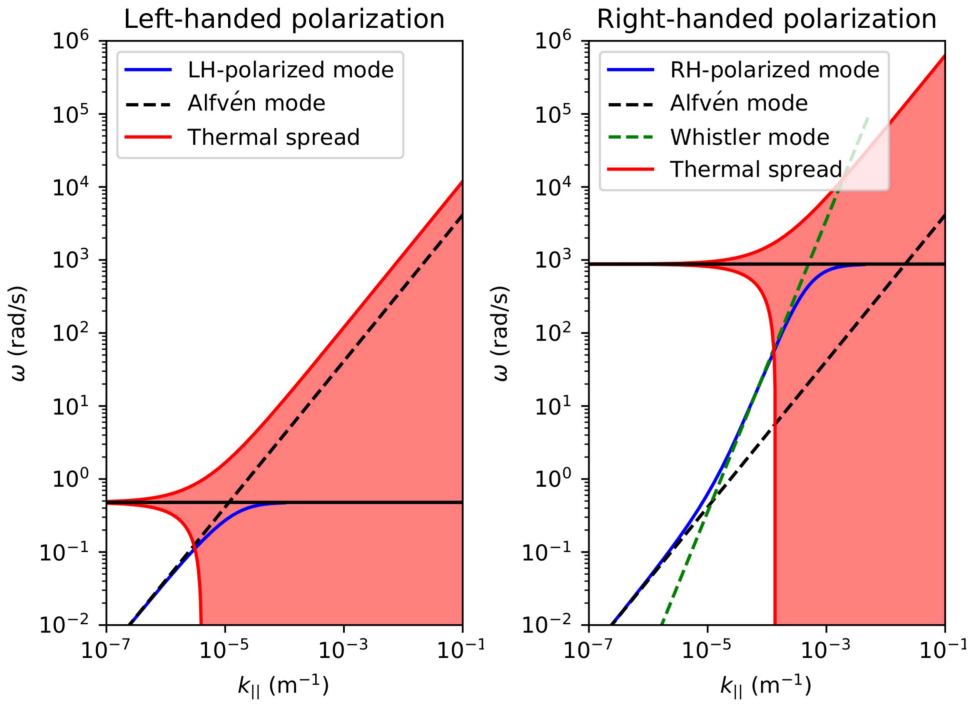

Figure 1. Dispersion equations, Equations (2) and (3), shown as the solid blue lines. The dashed lines show the case of non-dispersive Alfvén and Whistler modes, while the horizontal solid lines show Ω_p (left panel) and $|\Omega_e|$ (right panel). The shaded red region indicates the thermal spread of the plasma constituents: protons in the left panel and electrons in the right panel.

to get

$$\omega - \boldsymbol{k} \cdot \boldsymbol{v} = n\Omega, \tag{11}$$

with all quantities now specified in the bulk flow frame and $\boldsymbol{k}$ being the wave vector. As we only consider parallel propagating waves, this reduces to

$$\omega = n\Omega + k_{||} v_{||}, \tag{12}$$

which is the well-known result for resonance interactions in QLT (see, e.g., Schlickeiser 2002 and Shalchi 2009, among others) in the absence of dynamical effects. For our present application, Equation (12) will describe the resonance between dispersive wave modes, their frequency given by ω, resonating with thermal particles, their cyclotron frequency, Ω, Doppler-shifted by their parallel speed, $v_{||}$. For additional details concerning wave–particle resonances, see also, e.g., Steinacker & Miller (1992), Dröge et al. (1993), Vainio (2000), and Marsch (2006).

4. Cyclotron Resonance in Warm Plasmas

In Section 2, we assumed that $T_p = 0$, implying that $v_{||} = 0$ for the thermal protons in the plasma. Substitution into Equation (12) therefore gives the cyclotron resonance as $\omega_{\rm LH} = \Omega_p$, which is the behavior seen in the left panel of Figure 1. A similar resonance is seen in the right panel when $\omega_{\rm RH} = |\Omega_e|$. The question is now what happens if $T_p \neq 0$? Of course, as mentioned earlier, the wave dispersion relations may be altered, but, of special interest here is that $v_{||} \neq 0$, which, according to Equation (12), will change the resonant frequency.

Assuming that the thermal plasma particles follow a Maxwellian distribution, a representative choice for the speed at which thermal particles move along the field would be the most likely thermal speed,

$$v_{\rm th}^{p} = \sqrt{\frac{2k_{\rm B}T_p}{m_p}}, \tag{13}$$

with $k_{\rm B}$ Boltzmann's constant. A similar expression holds for the thermal speed $v_{\rm th}^{e}$ of the electrons. A more detailed calculation by Gary & Nishimura (2004), however, shows that we should instead adopt $3v_{\rm th}$, so that, with respect to the mean field, the majority of thermal particles move with a parallel speed of $v_{||} \in [-3v_{\rm th}, +3v_{\rm th}]$, the $\pm$ indicating the random nature of the particle velocity distribution.[3] Using Equation (3), the cyclotron resonance between protons and LH polarized waves, and therefore the damping of the LH waves by the thermal particles, will predominantly occur when

$$\omega_{\rm LH} \in \Omega_p \pm 3v_{\rm th}^{p} k_{||}. \tag{14}$$

This region, referred to as the "thermal spread" of the protons, is indicated by the red shaded region in the left panel of Figure 1. The right panel shows a similar filled region where the damping of RH polarized waves takes place,

$$\omega_{\rm RH} \in |\Omega_e| \pm 3v_{\rm th}^{e} k_{||}, \tag{15}$$

noting that, for RH modes, $n\Omega = -1(-|\Omega_e|) = |\Omega_e|$. The idea is now that any wave "passing through" (intersecting) this shaded region, where thermal particles resonate with parallel waves, will be heavily damped. The actual rate of damping is not of importance to us, only the value of $k_{||}$ where the onset of significant damping kicks in. In the turbulence nomenclature of the wavelike slab component, this value of $k_{||}$ is referred to as

[3] Formally, if there is a large temperature anisotropy in the plasma, we should use the parallel thermal speed, $v_{{\rm th},||}^{p}$, calculated using the parallel proton temperature, $T_{p,||}$.

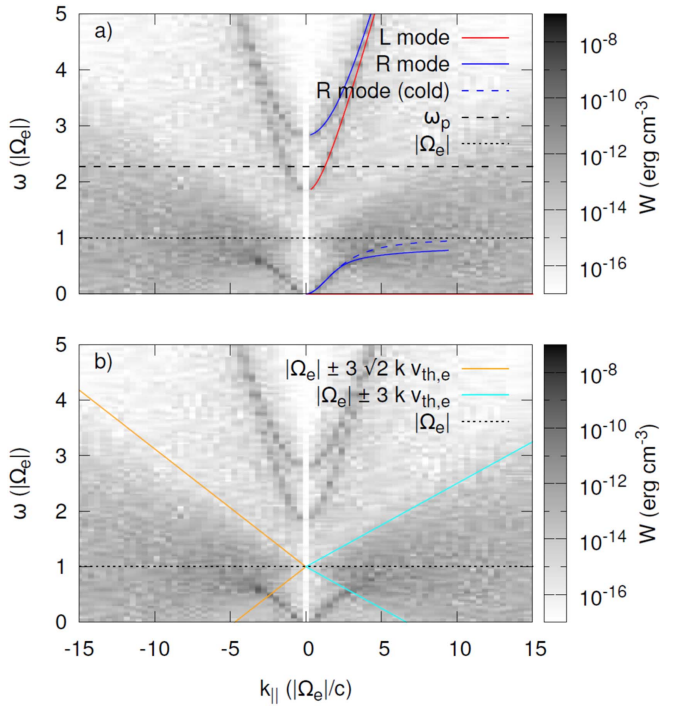

Figure 2. Results taken from Schreiner et al. (2017) showing a simulated right-handed polarized wave propagating along the mean field (top panel; referred to as the R mode). Note that the dispersion relations for both cold and warm plasmas are shown. The bottom panel is the same, but includes different choices of the thermal spread of the electrons in the plasma. Note that these authors use a different definition of $v_{\rm th}$ and hence have an additional factor of $\sqrt{2}$ in most expressions.

Table 1
The Assumed Solar Wind Conditions at 1 au

$B = 5$ nT
$n_p = n_e = 7$ #/cc
$T_p = 0.95 \times 10^5$ K
$T_e = 1.46 \times 10^5$ K
$\omega_e = 1.49 \times 10^5$ rad s^{-1}
$\omega_p = 3482$ rad s^{-1}
$\lvert\Omega_e\rvert = 878$ rad s^{-1}
$\Omega_p = 0.48$ rad s^{-1}
$v_{\rm th}^e = 2103$ km s^{-1}
$v_{\rm th}^p = 40$ km s^{-1}
$V_{\rm A} = 41$ km s^{-1}

the dissipation range onset wavenumber, denoted by k_d, and is discussed in detail in the next section.

The reasoning behind this motivation for temperature-modified cyclotron resonance was recently demonstrated by Schreiner et al. (2017), where these authors simulated the damping of RH polarized waves by a thermal plasma. Figure 2 shows their results (the gray contour plot) together with the relevant dispersion relationships (top panel) and the thermal spread of the plasma particles (bottom panel). Among other results, Schreiner et al. (2017) find a very effective damping of the RH modes once they enter this Doppler-shifted cyclotron resonance region. Note that they also considered the dispersive relationship at $\omega \gg |\Omega_e|$ (which we ignore) and show the dispersion relationship for both cold and warm plasmas (the solid and dashed blue lines in Figure 2). It is clear that the dispersive behavior is modified close to the cyclotron frequency, while, in our approach of assuming a cold plasma, we ignore this modification (see also the discussion by Dröge 2000). For our approach to therefore be valid, we require that the onset of resonance (see the next section) should occur at $\omega \ll \Omega$, which we discuss in the next section.

Lastly, up to now we considered only the effect of forward-moving waves, i.e., $k_{||} > 0$. In fact, Figure 1 shows that forward-moving waves resonate with backward-moving thermal particles. However, due to the symmetry of the situation, we have, to an equal extent, backward-moving waves being damped by forward-moving thermal particles, making this damping process independent of the wave propagation direction or cross-helicity.

5. The Onset of Damping

To find the onset wavenumber of the slab dissipation range, we find the smallest value of $k_{||}$ where the Doppler-shifted cyclotron resonance between dispersive waves and thermal particles occurs. Examining Figure 1, this is the intersection of the blue and red curves. We assume that the plasma is warm enough so that the resonance occurs below the cyclotron branch, but rather at the non-dispersive regime $\omega \ll \Omega$ (for a discussion of the case where particles resonate with the proton-cyclotron branch, see, e.g., Tan et al. 2011). For LH waves, $k_{d,\rm LH}$ can therefore be approximated as

$$V_{\rm A} k_{d,\rm LH} \approx \Omega_p - 3 v_{\rm th}^p k_{d,\rm LH}, \tag{16}$$

leading to

$$k_{d,\rm LH} \approx \frac{\Omega_p}{V_{\rm A} + 3 v_{\rm th}^p}. \tag{17}$$

This is similar to the expressions of Leamon et al. (1998b), but with the additional factor of 3. For the RH polarized waves, a resonance can either occur with the Alfvén or Whistler modes, giving either

$$k_{d,\rm RH}(T_e \gg T^*) \approx \frac{|\Omega_e|}{V_{\rm A} + 3 v_{\rm th}^e} \tag{18}$$

or

$$k_{d,\rm RH}(T_e \ll T^*) \approx \frac{3 v_{\rm th}^e \omega_e^2}{2c^2 |\Omega_e|}\left(\sqrt{1 + \left(\frac{2c|\Omega_e|}{3 v_{\rm th}^e \omega_e}\right)^2} - 1\right), \tag{19}$$

depending on the temperature of the plasma. The critical temperature can be determined by setting

$$V_{\rm A} k_{||}^* = c^2 (k_{||}^*)^2 \frac{|\Omega_e|}{\omega_e^2}, \tag{20}$$

and calculating T^* from

$$V_{\rm A} k_{||}^* = |\Omega_e| - 3\sqrt{\frac{2 k_{\rm B} T^*}{m_e}} k_{||}^*, \tag{21}$$

where a comparison with solar wind values at Earth indicates that $T_e \ll T^*$ (see, e.g., Newbury et al. 1998), and hence that Equation (19) should be used for RH modes.

Based on the results presented in Figure 1, $k_{||}^{d,\rm LH} < k_{||}^{d,\rm RH}$ and, if a spacecraft observes an (first) onset of the dissipation range, it would most likely correspond to $k_{||}^{d,\rm LH}$. We now compare our estimate of $k_{||}^{d,\rm LH}$ to the observations of Smith et al. (2012) and show this comparison in Figure 3. The data points of Smith et al. (2012) are shown as the blue circles,

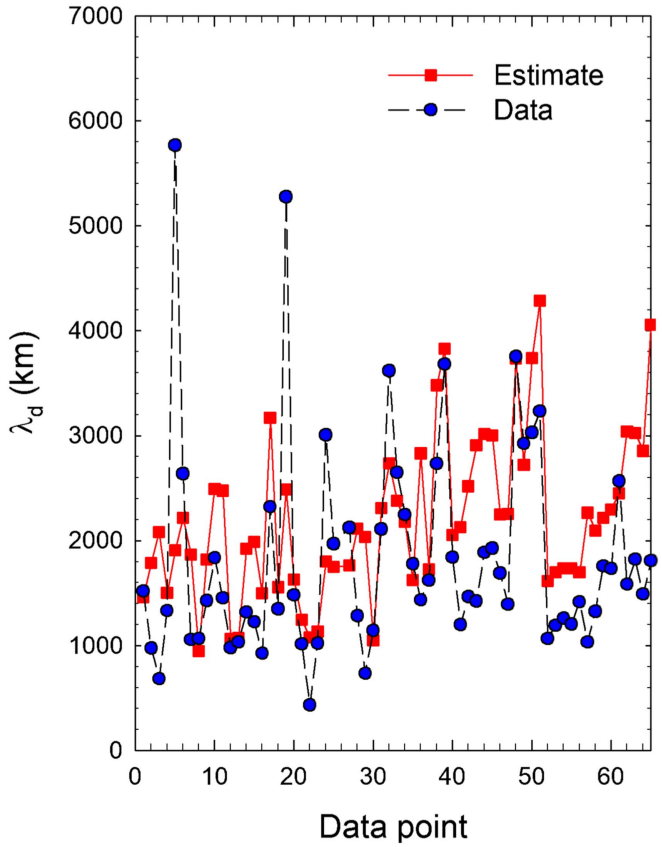

Figure 3. Comparison between our estimates of the onset of the turbulence dissipation range (red squares), with observations of the same reported by Smith et al. (2012), shown by the blue circles.

while our calculated value of λ^d is shown as the red squares. For the calculation of λ^d, we use all of the plasma parameters as reported by Smith et al. (2012), and set $\lambda^d = 2\pi/k_{||}^{d,\mathrm{LH}}$. Overall, a good comparison between the solar wind observations and theoretical calculation is evident, barring two outlying data points.

6. Implications for the Wave Spectrum and the Electron Inertial Range

Based on our calculations of $k_{||}^d$ described above, we can now set up a wavelike turbulence spectrum, as described by Equation (1), which has different dissipation range onsets for either LH polarized, $\sum\omega_{\mathrm{LH}}^j$, or RH polarized, $\sum\omega_{\mathrm{RH}}^j$, components. Figure 4 shows such an illustrative spectrum, where an energy-independent energy range is defined at low wavenumbers, a Kolmogorov-type inertial range at intermediate values (indicated on the figure as the filled regions), and, at larger wavenumbers, a dissipation range, where the energy dissipates as $\sim k_{||}^{-5}$. Note that each turbulence component may have a different value of $k_{||}^d$, and based on the results presented above, we expect $k_{||}^{d,\mathrm{LH}} < k_{||}^{d,\mathrm{RH}}$.

Lastly, we examine the combined, or total, slab spectrum, which is just a linear combination of the different polarized modes (see Equation (1)). Such a spectrum is shown in the left panel of Figure 5, focusing especially on the region close to the dissipation range onset. The composite spectrum shows two inflections, the first being where the onset of LH wave damping occurs, and the second, at larger values of $k_{||}$, where RH waves

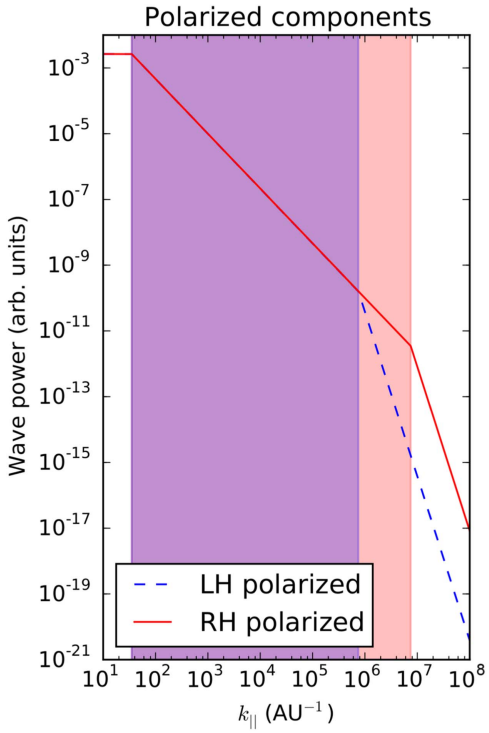

Figure 4. Illustrative turbulence spectrum showing how the wave energy will be distributed between LH and RH polarized wave components. Note that the dissipation range onset is different for different components.

are also starting to be significantly damped. Figure 5 is very reminiscent of the results of Alexandrova et al. (2009) and Sahraoui et al. (2009), which show indications of a second inertial range (referred to as the electron inertial range). In our present formulation, this second inertial range is formed due to the LH polarized wave components being damped, where, in this range of $k_{||}$, RH components still follow the cascade process. As expected, this will lead to a nonzero magnetic helicity spectrum, where we define the magnetic helicity as

$$\sigma_M := \frac{\sum_{j=\pm1}\omega_{\mathrm{LH}}^j - \sum_{j=\pm1}\omega_{\mathrm{RH}}^j}{\sum_{j=\pm1}\omega_{\mathrm{LH}}^j + \sum_{j=\pm1}\omega_{\mathrm{RH}}^j}. \tag{22}$$

The calculated σ_M is shown in the right panel of Figure 5 as a function of $k_{||}$. As expected, in the second inertial range, σ_M becomes negative, indicating an excess of RH wave modes. Again, this seems to be in general agreement with observations (see, e.g., Smith et al. 2006b; Hamilton et al. 2008)

7. Modeling the Solar Wind Proton and Electron Temperatures

The equations that govern the Oughton et al. (2011) model are given by (following the notation employed by Engelbrecht & Burger 2013a)

$$\frac{dZ^2}{dr} = -[1 + M\sigma_D - C_{\mathrm{sh}}^Z]\frac{Z^2}{r} - \frac{2\alpha f_{ZW}^+}{V_s}\frac{WZ^2}{l}\frac{1}{1 + Z/W} - \frac{\alpha f}{V_s}\frac{Z^3}{l} + \frac{2\alpha X^+}{V_s}, \tag{23}$$

$$\frac{dW^2}{dr} = -[1 + M\tilde{\sigma}_D - C_{\rm sh}^W]\frac{W^2}{r} - \frac{\tilde{\alpha}\tilde{f}}{V_s}\frac{ZW^2}{\lambda}\frac{2}{1+\lambda/l} - \frac{2\tilde{\alpha}(1-\tilde{\sigma}_c^2)}{V_s}\frac{W^4\lambda_{c,s}}{\lambda^2 V_{\rm A}} - \frac{2\alpha X^+}{V_s} + \frac{\dot{E}_{\rm PI}}{V_s}, \quad (24)$$

$$\frac{dl}{dr} = -C_{\rm sh}^Z\frac{l}{r} + \frac{\beta}{V_s}fZ + f_{ZW}^+\frac{\beta}{V_s}\frac{2W}{1+Z/W} - \frac{\beta}{V_s}\frac{2lX^+}{Z^2}, \quad (25)$$

$$\frac{d\lambda}{dr} = -C_{\rm sh}^W\frac{\lambda}{r} + \frac{2\tilde{\beta}}{V_s}\frac{\tilde{f}Z}{1+\lambda/l} + (1-\tilde{\sigma}_c^2)\frac{2\tilde{\beta}}{V_s}\frac{W^2\lambda_{c,s}}{\lambda V_{\rm A}} + \frac{2\tilde{\beta}}{V_s}\frac{\alpha\lambda X^+}{\tilde{\alpha}W^2}, \quad (26)$$

$$\frac{d\lambda_{c,s}}{dr} = -C_{\rm sh}^W\frac{\lambda_{c,s}}{r} + 2\tilde{\alpha}(1-\tilde{\sigma}_c^2)\frac{W^2\lambda_{c,s}^2}{V_s V_{\rm A}\lambda^2} - (\lambda_{c,s}-\lambda_{\rm res})\frac{\dot{E}_{\rm PI}}{V_s W^2}, \quad (27)$$

$$\frac{d\sigma_c}{dr} = \frac{\alpha}{V_s}\frac{f'Z}{l} + \frac{\alpha}{V_s}\frac{f'_{ZW}W}{l}\frac{2}{1+Z/W} - \frac{\alpha}{V_s}\frac{2(\sigma_c X^+ - X^-)}{Z^2} - \left[\frac{C_{\rm sh}^Z - M\sigma_D}{r}\right]\sigma_c, \quad (28)$$

$$\frac{d\tilde{\sigma}_c}{dr} = \frac{\tilde{f}'}{1+\lambda/l}\frac{2\tilde{\alpha}}{V_s}\frac{Z}{\lambda} + \tilde{\sigma}_c(1-\tilde{\sigma}_c^2)\frac{2\tilde{\alpha}}{V_s}\frac{W^2\lambda_{c,s}}{\lambda^2 V_{\rm A}} + \frac{2\alpha(\tilde{\sigma}_c X^+ - X^-)}{V_s W^2} - \left[\frac{C_{\rm sh}^W - M\tilde{\sigma}_D}{r} + \frac{\dot{E}_{\rm PI}}{V_s W^2}\right]\tilde{\sigma}_c, \quad (29)$$

where W^2 and Z^2 denote half the total fluctuation energies associated with the wavelike and quasi-2D components. Note that here the tildes denote quantities associated with the wavelike component. The variables l and λ denote perpendicular correlation scales associated with the wavelike and quasi-2D components, respectively, while $\lambda_{c,s}$ denotes the correlation scale parallel to the assumed uniform background heliospheric magnetic field (HMF). The normalized cross-helicity is denoted by σ_c. Note that V_s denotes the bulk solar wind velocity and $V_{\rm A}$ the Alfvén speed calculated from the global (assumed uniform) HMF and density fields. The quantities α and β are de Kármán-Taylor constants (see, e.g., Batchelor 1970). The normalized energy difference, denoted by σ_D, is a measure of the balance between the magnetic and kinetic energies implicit to the fluctuations considered (Bavassono et al. 1998; Breech et al. 2008; Perri & Balogh 2010; Zank et al. 2012; Bruno & Carbone 2013). The constants $C_{\rm sh}$ model shear effects, while the mixing factor M models the coupling of the small-scale fluctuations to gradients in large-scale fields (see, e.g., Breech et al. 2008 for more details).

The various quantities denoted by f are attenuation factors that model the weakening of nonlinear factors associated with larger values of the cross-helicities associated with the wavelike and quasi-2D components, and are related through

$$\begin{aligned} f &= f_{zz}^+ \\ \tilde{f} &= f_{wz}^+ \\ f' &= \sigma_c f_{zz}^+ - f_{zz}^- \\ \tilde{f}' &= \tilde{\sigma}_c f_{wz}^+ - f_{wz}^- \\ f_{zw}' &= \sigma_c f_{zw}^+ - f_{zw}^-, \end{aligned} \quad (30)$$

where, denoting z and w with the generic symbols a and b,

$$f_{ab}^{\pm} = \frac{1}{2}[(1+\sigma_c^a)\sqrt{1-\sigma_c^b} \pm (1-\sigma_c^a)\sqrt{1+\sigma_c^b}]. \quad (31)$$

The terms modeling the exchange of energy between the W and Z components are given by

$$X^{\pm} = \frac{1}{2}(Y^+ \pm Y^-), \quad (32)$$

where the quantities $Y^{\pm}$ are

$$Y^{\pm} = W_{\pm}Z_{\pm}\left[\frac{Z_{\mp}}{\lambda}\Gamma_w^{z_{\mp}w_{\pm}} + \frac{W_{\mp}}{\lambda}\Gamma_w^{w_{\mp}w_{\pm}} - \frac{Z_{\mp}}{l}\Gamma_w^{z_{\mp}z_{\pm}} - \frac{W_{\mp}}{l}\Gamma_w^{w_{\mp}z_{\pm}}\right]. \quad (33)$$

Furthermore,

$$\Gamma_c^{ab} = \frac{1}{1+\tau_{\rm nl}^{ab}/\tau_{\rm A}^c}, \quad (34)$$

where $\tau_{\rm nl}^{ab}$ and $\tau_{\rm A}^c$ are the nonlinear and Alfvén times, respectively. These quantities are expressed as (Oughton et al. 2006, 2011)

$$\begin{aligned} \tau_{\rm A}^w &= \frac{\lambda_{c,s}}{V_{\rm A}}, \\ \tau_{\rm nl}^{ww} &= \frac{\lambda}{W}, \\ \tau_{\rm nl}^{zz} &= \frac{l}{Z}, \\ \tau_{\rm nl}^{zw} &= \frac{\lambda}{Z}, \\ \tau_{\rm nl}^{wz} &= \frac{l}{W}. \end{aligned} \quad (35)$$

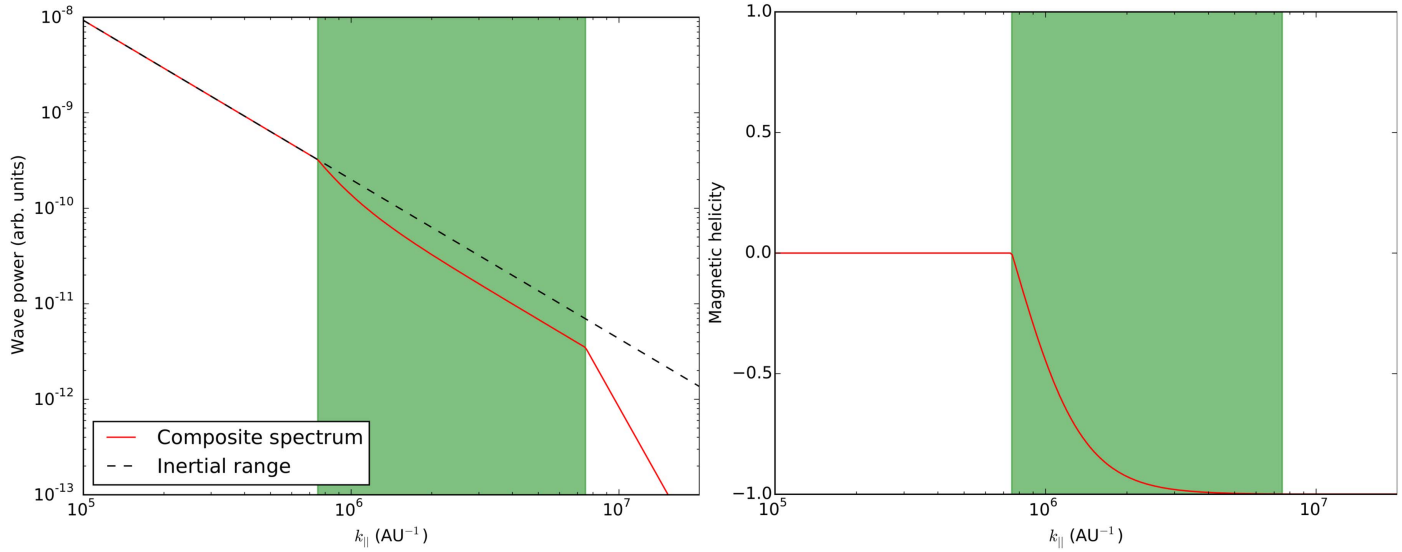

Figure 5. The left panel shows the composite slab spectrum (red line) near the dissipation range onset. A second inertial range is seen, indicated by the green filled region. The right panel shows the corresponding magnetic helicity spectrum.

For the proton and electron temperature equations, we follow the approach of Breech et al. (2009), who assume that the proton heating rate Q_p due to the turbulent cascade is some fraction f_p of the total heating rate Q, so that $Q_p = f_p Q$. Then, under the further assumption that the rest of this energy goes to the electrons, the electron heating rate will be $Q_e = (1 - f_p)Q$. Taking into account Coulomb collisions and electron heat flux, the temperature equations become

$$\frac{dT_p}{dr} = -\frac{4}{3}\frac{T_p}{r} + f_p\left[\frac{\alpha m_p}{3V_s k_B}\left(\frac{fZ^3}{l} + \frac{2f_{ZW}^{+}}{1+Z/W}\frac{WZ^2}{l}\right) + \frac{2\tilde{\alpha}m_p}{3V_s k_B}\frac{\tilde{f}}{1+\lambda/l}\frac{ZW^2}{\lambda} + \frac{2\tilde{\alpha}m_p}{3V_s k_B}(1-\tilde{\sigma}_c^2)\frac{W^4\lambda_{c,s}}{\lambda^2 V_A}\right] + \frac{T_e - T_p}{\tau_c V_s}, \tag{36}$$

$$\frac{dT_e}{dr} = -\frac{4}{3}\frac{T_e}{r} + (1-f_p)\left[\frac{\alpha m_p}{3V_s k_B}\left(\frac{fZ^3}{l} + \frac{2f_{ZW}^{+}}{1+Z/W}\frac{WZ^2}{l}\right) + \frac{2\tilde{\alpha}m_p}{3V_s k_B}\frac{\tilde{f}}{1+\lambda/l}\frac{ZW^2}{\lambda} + \frac{2\tilde{\alpha}m_p}{3V_s k_B}(1-\tilde{\sigma}_c^2)\frac{W^4\lambda_{c,s}}{\lambda^2 V_A}\right] - \frac{T_e - T_p}{\tau_c V_s} - \frac{2}{3V_s k_B n_p}\nabla\cdot\boldsymbol{q}_e, \tag{37}$$

with k_B the Boltzmann constant, n_p the proton density, and m_p the proton mass. Note that we, following Breech et al. (2009), ignore the effects of proton heat conduction and consider only the effects of electron heat conduction, modeled with the $\nabla\cdot\boldsymbol{q}_e$ term. Cranmer et al. (2009) argue, based on observations reported by Marsch et al. (1982), that the effect of proton heat conduction is considerably less than that of electron heat conduction (however, see Scudder 2015 for a counterargument). Lastly, proton–electron collisions are modeled with the $(T_e–T_p)/\tau_c V_s$ term, where τ_c denotes a Coulomb collision term.

We solve the TTM equations using a standard fourth-order Runge–Kutta numerical scheme for generic solar minimum conditions. During solar minimum, the solar wind speed displays a marked latitudinal dependence, with a speed of ~800 km s^{-1} over the solar poles and ~400 km s^{-1} in the ecliptic plane (see, e.g., McComas et al. 2000). This is modeled as a function of colatitude θ using a hyperbolic tangent function,

$$V_{sw}(\theta) = 400\begin{cases}\frac{3}{2} - \frac{1}{2}\tanh\left[8(\theta - \pi/2 + \alpha + \delta_t)\right], \theta \leqslant \pi/2; \\ \frac{3}{2} + \frac{1}{2}\tanh\left[8(\theta - \pi/2 - \alpha - \delta_t)\right], \theta > \pi/2\end{cases} \tag{38}$$

in km s^{-1}, with $\alpha = 5°$ the tilt angle of the heliospheric current sheet and $\delta_t = \pi/9$ radians. The factor of 8 simply governs the steepness of the transition of the function. The solar wind proton density n_p is assumed to scale as r^{-2} and is chosen to be 7/cc at Earth, decreasing toward the poles to a value of 2.5/cc at 1 au (see, e.g., McComas et al. 2000) according to a hyperbolic tangent function similar to Equation (38). We assume that the electron density is equal to that of the protons. Furthermore, we assume that the HMF is described by the Parker (1958) field, with a solar minimum magnitude of 5 nT at Earth.

The de Kármán-Taylor constants used here follow one of the values considered by Pei et al. (2010), where $\alpha = 0.125$. Assuming turbulent decay at constant Reynolds numbers then leads to $\alpha = 2\beta$ (Oughton et al. 2011). The geometrical mixing term is here, as in Breech et al. (2008), taken to be $M = \cos^2\psi$, where ψ is the HMF winding angle, calculated as that of the Parker (1958) heliospheric magnetic field (HMF). The normalized energy difference σ_D is assumed to be equal to $-1/3$, which implies an Alfvén ratio of 1/2, a reasonable value in the inner heliosphere (Roberts et al. 1987a, 1987b). Stream-shear

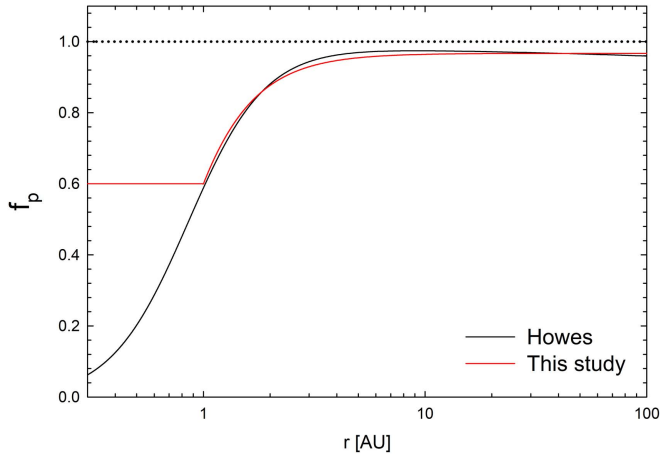

Figure 6. Fraction of turbulent energy f_p of the turbulent heat that goes to protons, as a function of radial distance. The black line indicates the fraction proposed by Howes (2010, 2011), and the red line the approximation to the aforementioned result employed in this study.

effects are modeled exactly as in Breech et al. (2008), under the assumption that the stream-shear constants for the wavelike and quasi-2D components are identical (Oughton et al. 2011; Engelbrecht & Burger 2013a). The pickup energy source term employed here is identical to that employed by Oughton et al. (2011), based on that used by, e.g., Smith et al. (2001) and Isenberg (2005),

$$\dot{E}_{\rm PI} = \zeta \frac{V_{\rm sw}^2 n_{\rm H}}{\tau_{\rm ion} n_{\rm sw}} \exp\left[-(L_{\rm cav}/r)(\theta_n/\sin\theta_n)\right]. \quad (39)$$

where ζ, chosen to equal 0.04 after Oughton et al. (2011), represents the fraction of pickup-ion energy that goes to the generated fluctuations, $L_{\rm cav} = 5.6$ au the size of the ionization cavity (from, e.g., Isenberg 2005), $n_{\rm sw}$ the solar wind proton density, $n_H = 0.1$/cc the neutral hydrogen density (from Breech et al. 2008; Oughton et al. 2011), and $\tau_{\rm ion} = 1.97 \times 10^6$ s the ionization time (from Engelbrecht & Strauss 2015). The angle θ_n is measured between an observation point and the neutral hydrogen upstream direction. As such, we mostly follow Engelbrecht & Burger (2013a) as to our choices for these quantities. The resonant length scale $\lambda_{\rm res}$ represents the scale at which some of the energy due to pickup-ion formation is injected into the wavelike fluctuation spectrum, and is modeled here as a function of the proton gyrofrequency, following Oughton et al. (2011), as $(2\pi\ V_{\rm sw})/\Omega_{\rm ci}$.

As to the electron conduction and collision terms in the temperature equations, for the former we follow the approach taken by Cranmer et al. (2009), who present weighted fits to *Helios* and *Ulysses* observations of the same (see, e.g., Marsch et al. 1982; Pilipp et al. 1990; Scime et al. 1994). This fit is given by

$$\ln\left(\frac{q_{\parallel,e}}{q_o}\right) = -0.7032 - 2.115x - 0.2545x^2, \quad (40)$$

with $q_o = 0.01$ erg cm^2 s^{-1} and $x = \ln(r/1\ {\rm au})$. Note that Equation (40) is essentially a fit to observations limited to the very inner heliosphere, and that caution needs to be exercised in the interpretation of results calculated using extrapolations

Table 2
Boundary Values Assumed at 0.3 au for the Oughton et al. (2011) TTM

Quantity	Unit	Ecliptic Values	Polar Values
Z^2	km^2 s^{-2}	1250	1600
W^2	km^2 s^{-2}	350	2000
λ	au	0.004	0.015
l	au	0.004	0.015
$\lambda_{c,s}$	au	0.011	0.011
σ_c	none	0.6	0.8
$\tilde{\sigma}_c$	none	0.6	0.8
T_p	K	4×10^5	2×10^6
T_e	K	7×10^5	7×10^5

thereof to larger radial distances. Furthermore, we follow Breech et al. (2009) in the assumption that Equation (40) holds for all latitudes, an assumption motivated by observations of this quantity analyzed by Scime et al. (1999), who reported no significant variation in $q_{\parallel,e}$ as observed by *Ulysses* as that spacecraft moved from fast to slow solar wind streams. The Coulomb collision frequency used is the approximation of Cranmer et al. (2009), where

$$\nu_e \approx 8.4 \times 10^{-9} \frac{n_e}{2.5\ {\rm cm}^{-3}} \frac{T_p}{10^5\ {\rm K}}. \quad (41)$$

Lastly, the quantity f_p, the fraction of heat due to the cascade of turbulent energy that goes to protons, needs to be modeled. Breech et al. (2009) report that a constant value of 0.6 leads to a reasonable agreement of the results of the Breech et al. (2008) TTM with *Ulysses* data. Cranmer et al. (2009) empirically derive proton and electron heating rates from *Helios* and *Ulysses* data, finding, in agreement with Breech et al. (2009), that $f_p = 0.6$ in the inner heliosphere. However, Cranmer et al. (2009) also report that f_p increases to a value of 0.8 at $\sim$5 au (see also Cranmer & van Ballegooijen 2012). Furthermore, these authors report only a weak latitudinal dependence for f_p. Howes (2010) calculates the relative electron and proton heating due to a turbulent cascade in a fully ionized, weakly collisional plasma, finding that

$$\frac{Q_p}{Q_e} = c_1 \frac{c_2^2 + \beta_p^\alpha}{c_3^2 + \beta_p^\alpha} \sqrt{\frac{m_p T_p}{m_e T_e}} \exp\left[-1/\beta_p\right], \quad (42)$$

where β_p is the proton plasma beta, $\alpha = 2 - 0.2 \log Tp/T_e$, $c_1 = 0.92$, $c_2 = 1.6 T_e/T_p$, and $c_3 = 18 + 5 \log Tp/T_e$. This result, when implemented using fits to electron and proton temperature observations, as shown in Figure 6 (black line), was reported by Howes (2011) to be in reasonably good agreement with the findings of Cranmer et al. (2009) as to f_p beyond 1 au. At radial distances less than 1 au, however, Equation (42) yields results far below the value of 0.6 reported by both Breech et al. (2009) and Cranmer et al. (2009). Due to this, we employ an approximate expression for f_p in this study based in part on the Howes (2010) result so as to achieve a consensus model for this quantity. Furthermore, although this quantity should in principle be a function of basic turbulence quantities yielded by the TTM (see, e.g., Matthaeus et al. 2016), an approximate approach greatly simplifies the analysis

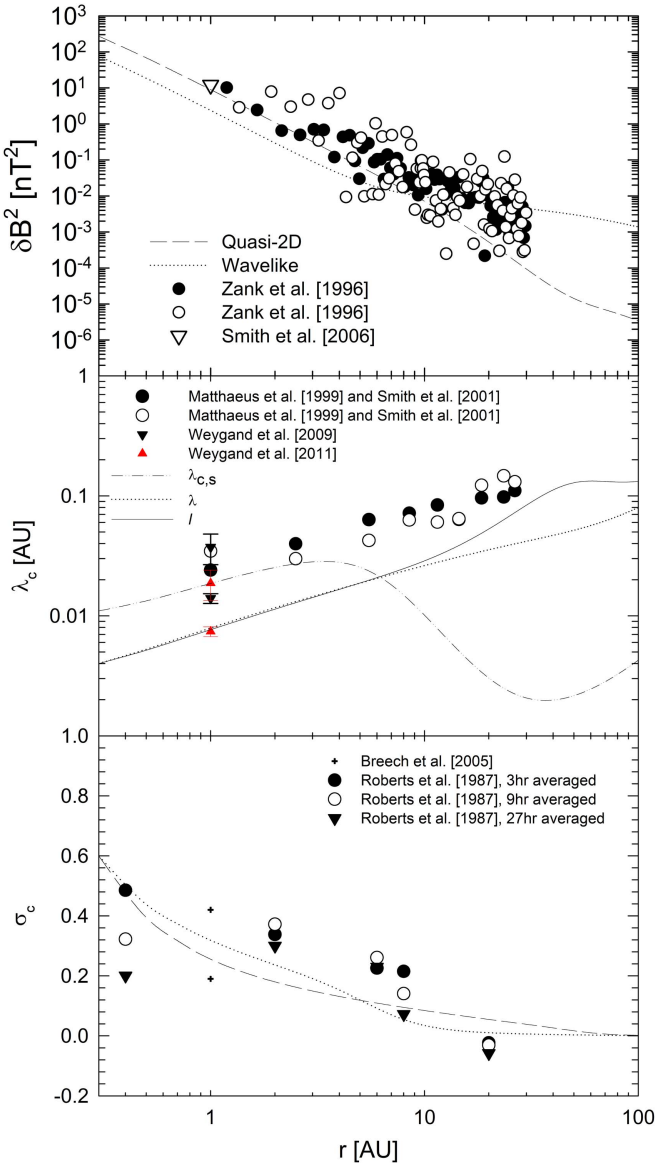

Figure 7. Variances (top panel), correlation scales (middle panel), and normalized cross-helicities (bottom panel) yielded by the Oughton et al. (2011) TTM as a function of heliocentric radial distance in the ecliptic plane. The above quantities are shown with relevant observations, with magnetic variances as reported by Zank et al. (1996) and Smith et al. (2006a); correlation scales as reported by Matthaeus et al. (1999), Smith et al. (2001), and Weygand et al. (2009, 2011); and normalized cross-helicities as reported by Breech et al. (2005), Roberts et al. (1987a1987b).

which follows. This approximation is given by

$$f_p = \begin{cases} 0.6, \; r \leqslant 1\text{au}; \\ 1.367 \exp\left[-1/(3.2r^{2.2})\right] - 0.4, \; r > 1\text{au}, \end{cases} \quad (43)$$

and shown as the red line in Figure 6. In the next section, the various results of the TTM discussed above will be presented, and the sensitivity of the temperature profiles to various modeled factors, such as the electron heat conductivity, will be discussed.

8. Temperature Modeling Results

The choices of initial boundary values at 0.3 au for the Oughton et al. (2011) TTM, listed in Table 2, are motivated by

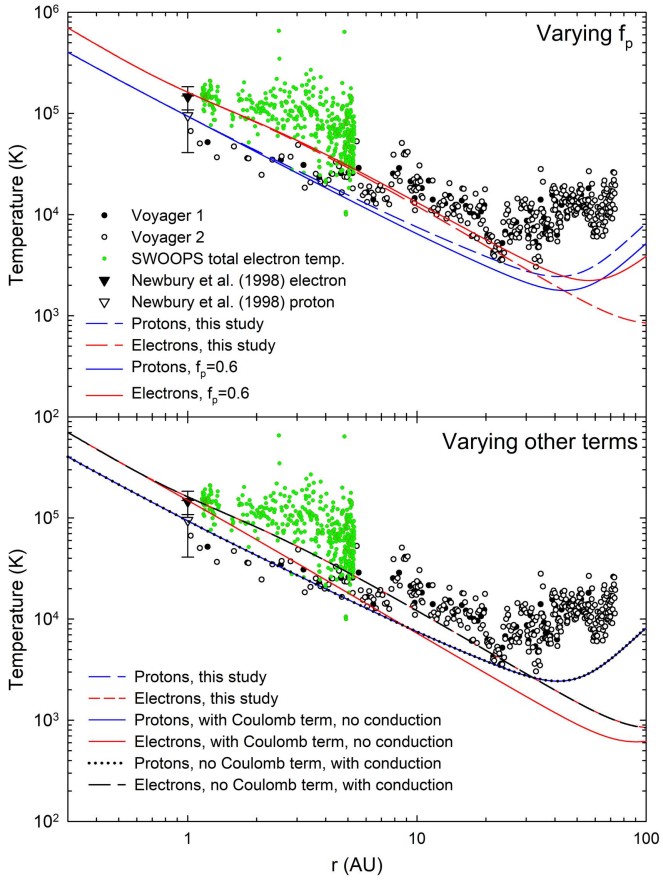

Figure 8. Electron and proton temperatures yielded by the Oughton et al. (2011) turbulence transport model in the ecliptic plane as a function of heliocentric radial distance. The *Voyager 1* and *2* proton temperature observations shown (black and white circles, respectively) are those reported by Smith et al. (2001), while the green dots are SWOOPS observations for the total electron temperature taken during *Ulysses*' sojourn in the ecliptic plane. Observations shown at 1 au are those of Newbury et al. (1998).

the requirement that the results yielded by the said model should agree with spacecraft observations, in the same way as discussed and implemented by Engelbrecht & Burger (2013a). Note, however, that some of the boundary values used here differ from those employed by Engelbrecht & Burger (2013a), so as to improve agreement with observations. In the solar ecliptic plane, boundary values are set so that the TTM yields correlation scales in agreement with the findings of Weygand et al. (2011) at Earth, as well as yielding a ratio of $Z^2/W^2 \approx 80/20$, in accordance with, e.g., Bieber et al. (1994). The ecliptic results for the magnetic variances calculated from the fluctuation energies, the correlation scales, and the normalized cross-helicities are shown as functions of heliocentric radial distance in Figure 7, along with various spacecraft observations. The variances and normalized cross-helicities are in reasonably good agreement with observations. The perpendicular correlation scales follow the radial trend of the Matthaeus et al. (1999) and Smith et al. (2001) *Voyager* observations well enough, but remain below them. This, however, may be due to the fact that correlation scales calculated using data gathered by a single spacecraft tend to be overestimated by a factor of two to four (Matthaeus et al. 2005).

Proton and electron temperatures yielded by the TTM as a function of heliocentric radial distance in the solar ecliptic

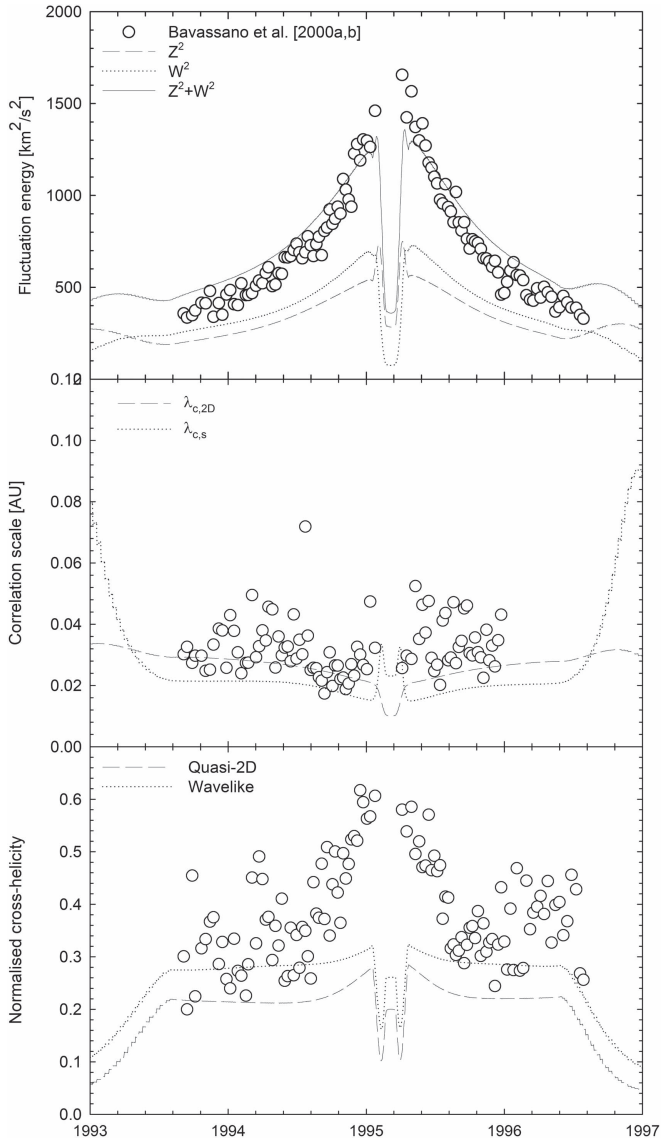

Figure 9. Turbulence quantities yielded by the Oughton et al. (2011) turbulence transport model, taken along the trajectory of *Ulysses*. These include fluctuation energies (top panel), correlation scales (middle panel), and normalized cross-helicities (bottom panel) with *Ulysses* observations reported by Bavassono et al. (2000a, 2000b). The bottom panels of Figure 10 show the corresponding radial and colatitudinal position of the *Ulysses* spacecraft as a function of time.

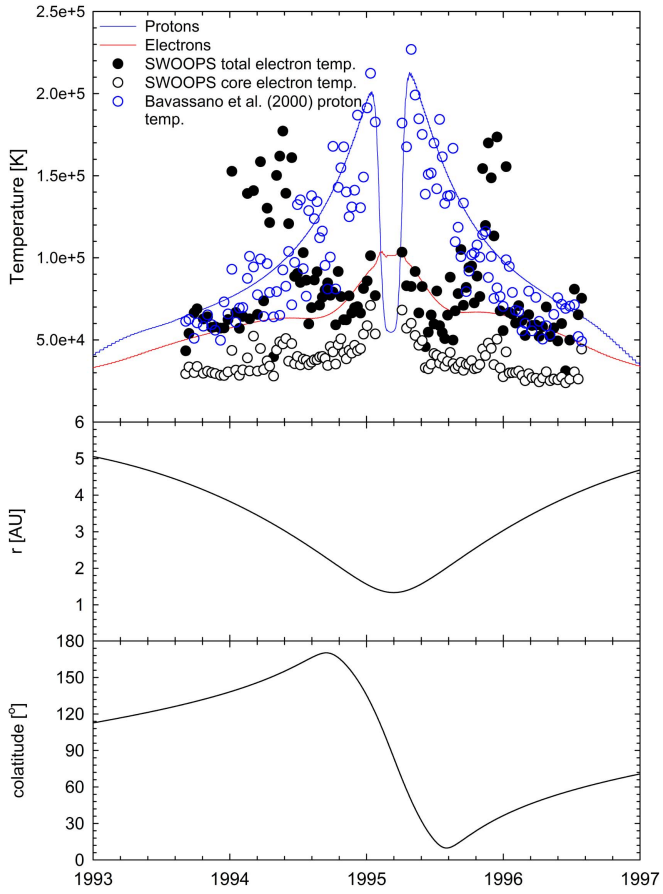

Figure 10. Electron and proton temperatures yielded by the Oughton et al. (2011) turbulence transport model, taken along the trajectory of *Ulysses* (top panel). The proton temperature observations shown (blue circles) are those of Bavassono et al. (2000a, 2000b), while electron data are SWOOPS observations for both the total (solid black circles) and core (white circles) electron temperatures corresponding to the proton temperature data intervals. The bottom panels show the corresponding radial and colatitudinal positions of the *Ulysses* spacecraft as a function of time.

plane are shown in Figure 8. The top panel of this figure shows the effects of varying f_p, assuming either a constant value of 0.6 for this quantity, as was done by Breech et al. (2009), or allowing it to vary radially by using Equation (43). Below 1 au, the electron and proton temperature radial dependences are the same and display a power-law dependence of $\sim r^{-4/3}$, steeper than that reported in the literature (see, e.g., Sittler & Scudder 1980; Phillips et al. 1995). However, at 1 au both proton and electron temperatures are within the error margins of the observed temperatures reported by Newbury et al. (1998). Further on, the solutions show the $\sim r^{-4/3}$ radial dependence reported by, e.g., Meyer-Vernet & Issautier (1998) and Richardson et al. (1995), out to about 10 au. Within this radial distance, the model agreement of the proton temperatures with spacecraft observations is reasonably good. Modeled electron temperatures follow the trend of the *Ulysses* SWOOPS data shown, but remain below observations. This may be due to the fact that the current model does not take into account electron heating due to interactions of electrons with solar wind bulk velocity jumps (see, e.g., Chashei & Fahr 2014a, 2014b). Beyond approximately 5–6 au, proton and electron temperatures for the case where $f_p = 0.6$ and Equation (43) begin to diverge, with electron temperatures for the latter choice of f_p showing a steady decrease as function of radial distance out to 100 au, while electron temperatures computed assuming that $f_p = 0.6$ show a turnup at $\sim$70 au, reminiscent of what is seen for both cases in the behavior of the proton temperatures. This is due to the action of the pickup-ion term (Equation (39)) in the TTM, which acts to inject energy into the wavelike component. From Figure 6, it can be seen that the use of Equation (43) to model f_p leads to only a tiny proportion of this energy heating the electrons, as opposed to the $f_p = 0.6$ case, where the electrons receive 40% of this energy. This then is also the reason why the proton temperature for this case is higher than that for the case of $f_p = 0.6$ at these large radial distances. Turning again to radial distances smaller than 1 au, the choice of f_p does not affect the electron temperatures, even if f_p is set to 1 (not shown), which implies no turbulent heating of the electrons. This implies that, at these radial distances, and up to $\sim$4 au, electron heating is dominated by the nonturbulent

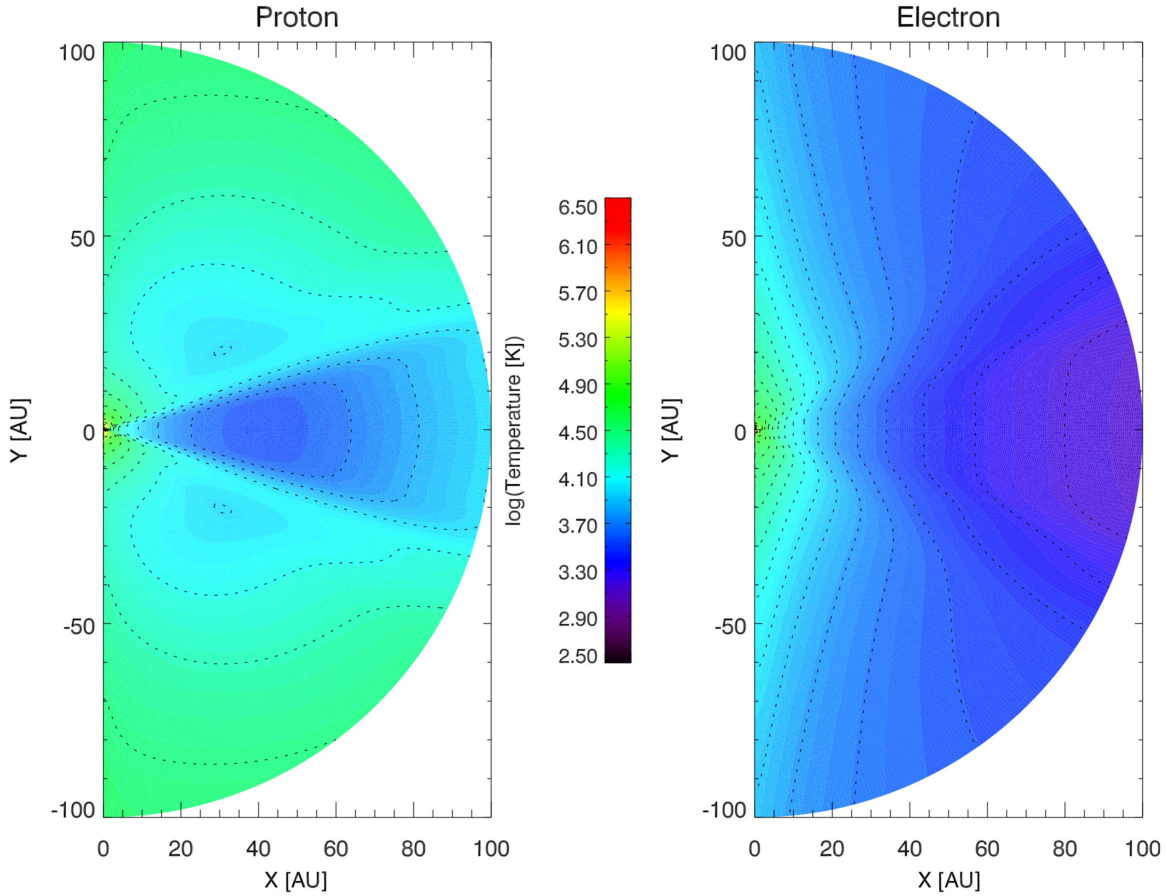

Figure 11. Meridional slice taken at 0° azimuth of the logarithm of the proton (left panel) and electron (right panel) temperatures yielded by the TTM.

terms in Equation (37). This is in line with what is reported by Štverák et al. (2015) from their analysis of electron cooling rates using *Helios* observations.

The bottom panel of Figure 8 shows the effects of switching off the Coulomb and heat conduction terms in Equation (37), again as a function of radial distance in the ecliptic plane. Note that the solutions shown in this panel are compared to the reference solutions computed with f_p modeled as in Equation (43) (dashed lines). When only the Coulomb term is active, electron temperatures, which are identical to the reference solutions, remain well below those computed, taking into account the heat conduction term. The negligible effect of collisions in this model has some contrast with the results of Breech et al. (2009), who employ a larger collision mean free path than Cranmer et al. (2009), and subsequently this study. Overall, from Figure 8 it can be seen that the heat conduction term plays a more significant role in the heating of electrons. Even though the heat conduction term has a stronger effect in terms of a slower decrease in the electron temperature with radial distance beyond ∼5 au, from the bottom panel of Figure 8 the marked "shelf" in electron temperatures as reported by Breech et al. (2009) cannot clearly be seen. This may be a consequence of the latitude at which these solutions are displayed. Proton results are not affected by changes in either of the terms, as collisions have a negligible effect and proton heat conduction is ignored in this study.

Due to the considerable excursions in latitude made by the *Ulysses* spacecraft, comparisons of TTM outputs with

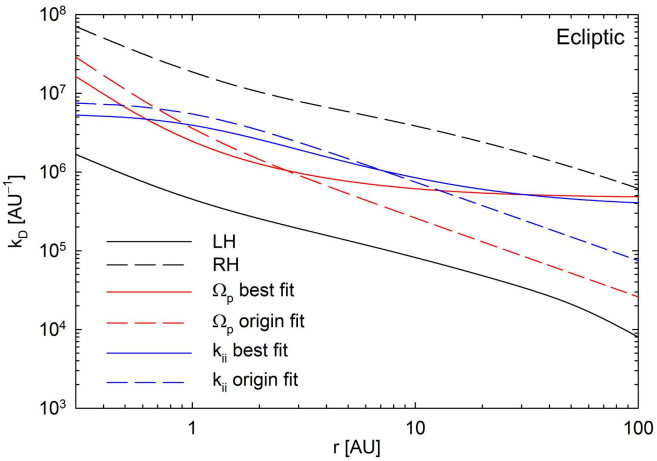

Figure 12. Dissipation range onset wavenumbers yielded by the various Leamon et al. (2000) models, as well as by Equations (17) and (19), as a function of radial distance in the solar ecliptic plane.

observations taken by that spacecraft need to be made along the actual trajectory of *Ulysses*. The Oughton et al. (2011) model is solved here in the usual manner, along radial spokes at different constant latitudes on a 3D grid, with points corresponding to *Ulysses*' trajectory being chosen and plotted as a function of time in Figures 9 and 10. The radial and colatitudinal positions of that spacecraft are shown as a function of time in the bottom panels of the latter figure, while

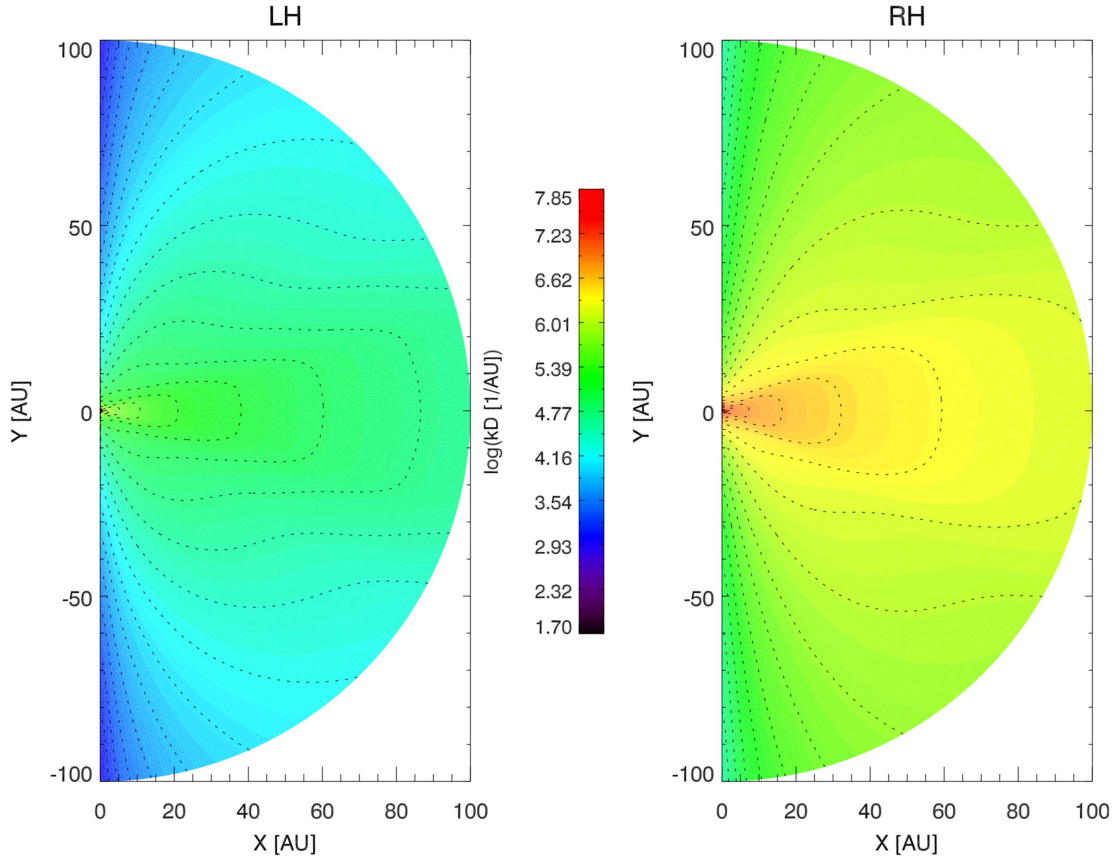

Figure 13. Meridional slice taken at 0° azimuth of the logarithm of the dissipation onset wavenumber for LH waves (Equation (17), left panel) and RH waves (Equation (19), right panel).

the former shows the variances, correlation scales, and normalized cross-helicities along with observations of the same reported by Bavassono et al. (2000a, 2000b). The results shown here with respect to these quantities are very similar to those reported by Engelbrecht & Burger (2013a). The total variance as well as the correlation scales yielded by the TTM are in reasonably good agreement with observations. However, the normalized cross-helicities do not agree well with observations. This may be due to the fact that boundary values in the ecliptic plane were chosen so as to yield results in agreement with observations for this quantity calculated for turbulent fluctuation spectra taken over periods of three or more hours, while the Bavassono et al. (2000a, 2000b) values were calculated for hourly averaged data. The electron and proton temperatures yielded by the TTM along *Ulysses*' trajectory are shown in Figure 10 along with observations of the electron total and core temperatures taken by the SWOOPs instrument, as well as the proton temperatures reported by Bavassono et al. (2000a, 2000b). For the purposes of comparison, electron temperature data taken at the same times as the proton temperatures are shown. As in Engelbrecht & Burger (2013a), the modeled proton temperatures agree well with observations. Modeled electron temperatures follow the trend of the observations, except at intermediate latitudes, where there is considerable scatter in the data. As these are the latitudes at which the transition from slow to fast solar wind occurs, better agreement with observation may be achieved by taking into account solar wind bulk velocity jumps as proposed by Chashei & Fahr (2014a, 2014b).

Figure 11 illustrates the broader spatial dependences of the proton and electron temperatures, and represents a meridional slice taken at constant longitude of these quantities. For examples of such slices for the turbulence quantities yielded by the Oughton et al. (2011) TTM, see Engelbrecht & Burger (2015). The proton temperatures (left panel) show a marked dependence on latitude, assuming higher values over the poles than in the ecliptic plane. Generally, these temperatures initially decrease as a function of radial distance, increasing again in the outer heliosphere due to the action of the pickup-ion term, although this effect is much more marked in the ecliptic plane. Electron temperatures decrease as a function of radial distance, as seen in Figure 8, due to the fact that the form for f_p employed here approaches unity at larger radial distances, so that the electrons are not very effectively heated due to the turbulent cascade of fluctuation energy generated by pickup ions. Electron temperatures over the poles tend to be higher than in the ecliptic plane, reflecting the larger variances at low latitudes. At intermediate latitudes, there is evidence of the so-called "shelf" region reported by Breech et al. (2009), which is also in the model related to the electron heat conduction term in Equation (37) presented here.

The following section considers the effects of using the electron and proton temperatures yielded by the Oughton et al. (2011) TTM as inputs for the expressions for the dissipation range onset wavenumber (Equations (17) and (19)) in Section 5. These results will be compared with extrapolations of the models for this quantity as considered by Leamon et al. (2000).

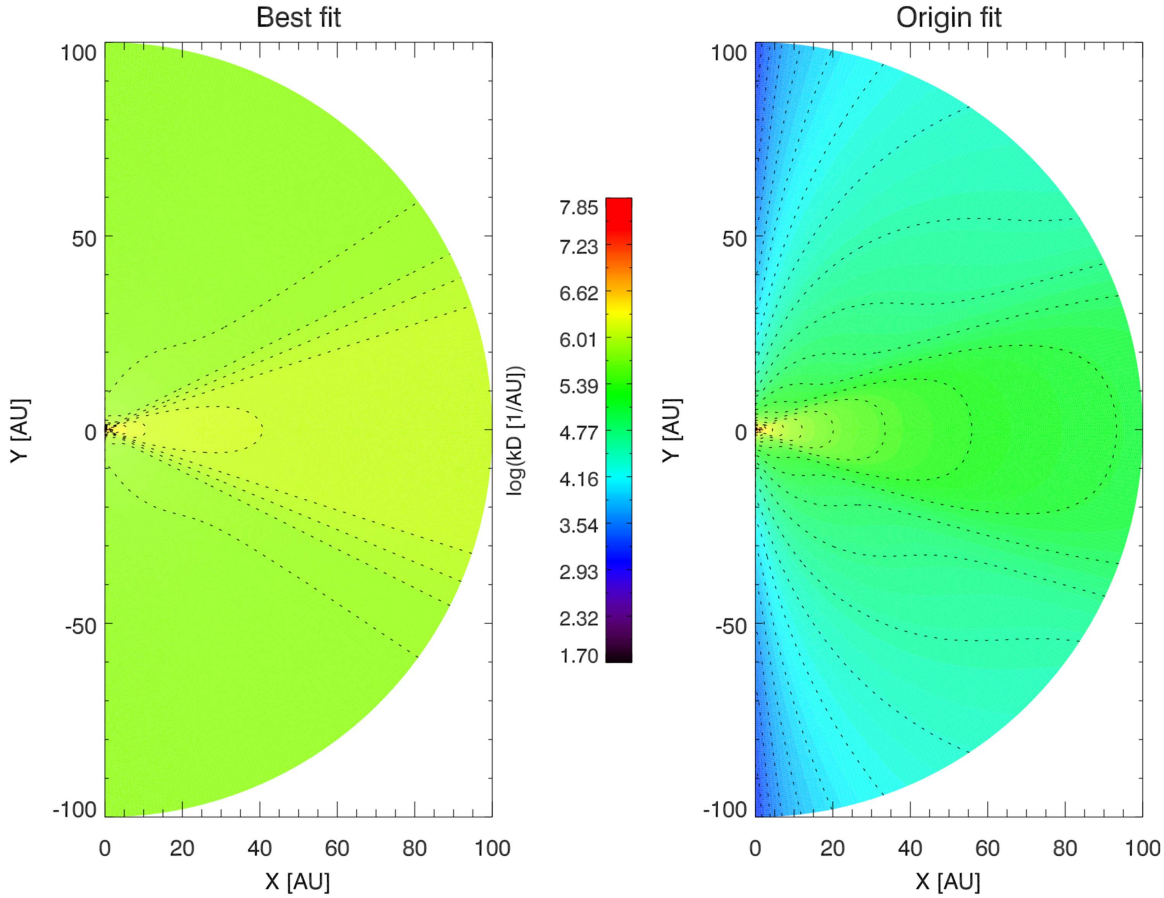

Figure 14. Meridional slice taken at 0° azimuth of the logarithm of the dissipation onset wavenumber assuming the proton gyrofrequency model for the extrapolated best-fit (left panel) and origin-fit models of Leamon et al. (2000).

9. Effects of Turbulence Transport on the Dissipation Range Onset Wavenumber

In order to compare the behaviors of the dissipation range onset wavenumber expressions proposed in this study, we consider extrapolations of the model fits to *Wind* observations at Earth proposed by Leamon et al. (2000) in the same way as done by Engelbrecht & Burger (2010, 2013b). Leamon et al. (2000) provide fits to observations under the assumption that either k_d is a function of the proton gyrofrequency, of the ion inertial scale, such that Engelbrecht & Burger (2010, 2013b)

$$k_D = \frac{2\pi}{V_{\rm sw}}(a_L + b_L \Omega_{\rm ci}), \tag{44}$$

or

$$k_D = \frac{2\pi}{V_{\rm sw}}\left(a_L + \frac{b_L}{2\pi} k_{ii} V_{\rm sw}\right), \tag{45}$$

respectively, with

$$k_{ii} = \frac{2\pi\Omega_{\rm ci}\sin\Psi}{V_{\rm A}}, \tag{46}$$

and Ψ the winding angle of the heliospheric magnetic field. For more details, see e.g., Bruno & Carbone (2013) and Parashar et al. (2015). Furthermore, the quantities a_L and b_L denote regression constants as reported by Leamon et al. (2000). In what is to follow, the phrase "origin fit" refers to the case where $a_L = 0$, whereas the phrase "best fit" refers to the values acquired by these authors for the fit parameters that yield the best χ^2 parameters. The extrapolations of the above models for k_d, along with the expressions derived in this study (Equation (17), referred to as "LH" and Equation (19), referred to as "RH"), are shown as functions of radial distance in the ecliptic plane in Figure 12. The extrapolations are done for exactly the same generic solar minimum conditions as are used in the TTM, as discussed in Section 7. As expected, the LH dissipation range onset wavenumber remains consistently larger than the RH k_d, differing by almost two orders of magnitude and showing a remarkably similar radial dependence in the ecliptic plane. When compared with the LH and RH results, the Leamon et al. (2000) k_d expressions yield considerably different values for this quantity throughout most of the heliosphere, barring the values yielded by the best-fit expressions in the very outer heliosphere, with considerable differences between these models and the LH results of this study at 1 au. However, given the considerable variability in reported observational values for k_d (see, e.g., Leamon et al. 1998b, 2000; Alexandrova et al. 2008; Hamilton et al. 2008; Bourouaine et al. 2012; Smith et al. 2012), this disagreement does not disqualify the approach we take in this study. Beyond ~20 au, the best-fit Leamon et al. (2000) k_d values become approximately constant, due to the fact that the regression constants b_L dominate both Equations (44) and (45),

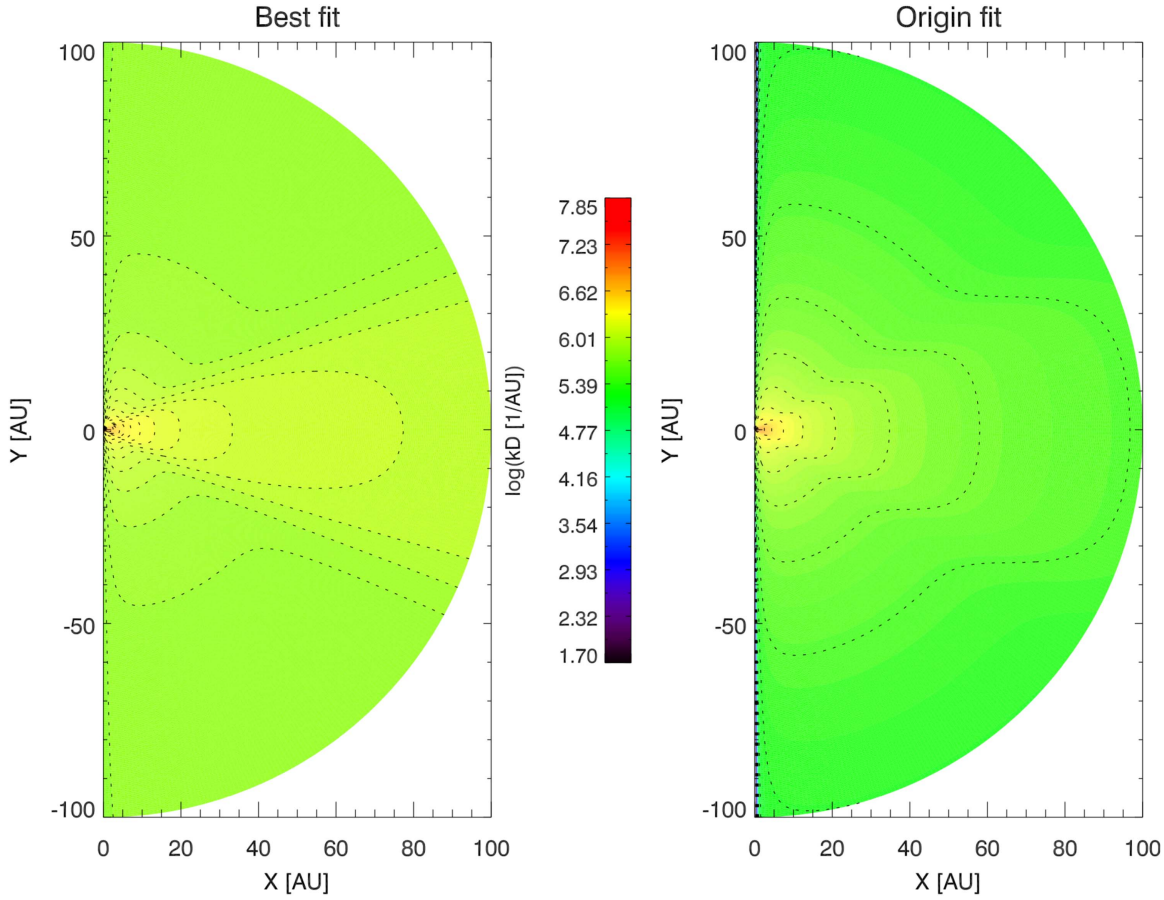

Figure 15. Meridional slice taken at 0° azimuth of the logarithm of the dissipation onset wavenumber assuming the ion inertial scale model for the extrapolated best-fit (left panel) and origin-fit models of Leamon et al. (2000).

which, in the absence of these constants (the origin-fit cases), yield considerably smaller values for k_d in the outer heliosphere. Both origin-fit cases display similar $\sim r^{-1}$ dependences in the outer heliosphere, which greatly resembles the radial dependences of the LH and RH cases. This may be due to the fact that the proton gyrofrequency, of which both origin fits are functions, plays a dominant role in both Equations (17) and (19). For the purposes of a broader comparison, meridional contours are shown for Equations (17) and (19), as well as the proton gyrofrequency and the ion inertial scale models for k_d in Figures 13–15, respectively. Overall, the behavior of Equation (17) mimics most closely that of the origin-fit proton gyrofrequency expression, with minor differences in their colatitudinal dependences. The other Leamon et al. (2000) models appear to vary only slightly with colatitude. Equation (19), on the other hand, assumes values close to those of both the best-fit Leamon et al. (2000) models in the outer heliosphere, but otherwise does not resemble any of these models in terms of its spatial dependences.

10. Discussion

Tractable approximations for the dissipation range onset wavenumber on the slab turbulence power spectrum have been derived based on the dissipation of LH and RH polarized waves. These approximations were shown to yield results in qualitative agreement with 1 au observations of this quantity reported by Smith et al. (2012). Furthermore, as the k_d for the RH waves was found to be uniformly larger than that for the LH waves, we expect the former quantity to represent the onset of a second, so-called electron dissipation range, in qualitative agreement with observations reported by, e.g., Alexandrova et al. (2009). The resulting nonzero helicity expected of such a spectrum is again in qualitative agreement with observations of the same (e.g., Hamilton et al. 2008).

The approximations here derived for k_d are functions of the solar wind proton and electron temperatures. To study the behavior of k_d throughout the heliosphere, we employ a two-component TTM, that of Oughton et al. (2011), to model these temperatures, following broadly the approach of Breech et al. (2009). The temperatures so acquired are in reasonable agreement with spacecraft observations at Earth (e.g., Newbury et al. 1998), those observed by the *Voyager* spacecraft (e.g., Richardson et al. 1995), and along the trajectory of *Ulysses* (e.g., Bavassono et al. 2000a, 2000b), providing a reasonable estimate of the spatial variations of the proton and electron temperatures in the supersonic solar wind. These results were then used to characterize the approximations for the dissipation range onset wavenumber derived in this study, as well as to compare these results with extrapolations of models for this quantity fitted to 1 au observations by Leamon et al. (2000) that have been employed in earlier galactic cosmic-ray electron modulation

studies. Results indicate that the values derived here for RH and LH waves bound the Leamon et al. (2000) extrapolations, with the dissipation range onset wavenumber corresponding to the LH waves generally being lower and following a broad spatial dependence similar to that for k_d modeled as a function of the proton gyrofrequency, albeit with a somewhat different latitudinal dependence. This latter point is in agreement with the conclusion drawn in the modulation study of Engelbrecht & Burger (2013b), who find the best agreement of their computed galactic cosmic-ray electron intensities with spacecraft observations at Earth when they employ such a model for k_d. This study therefore provides a reasonable estimate of the dissipation range onset wavenumber that can be extrapolated beyond 1 au, and therefore be employed in various charged particle transport studies. Given the sensitivity of the transport coefficients of low-energy galactic, Jovian (e.g., Ferreira et al. 2001a, 2001b; Strauss et al. 2011), and solar energetic (e.g., Strauss et al. 2017) electrons to the behavior of k_d, further studies are required to test the consequences of using the models presented here for this quantity on electron transport.

This work is based on the research supported wholly by the National Research Foundation of South Africa (grant No. 111731). Opinions expressed and conclusions arrived at are those of the authors and are not necessarily to be attributed to the NRF. N.E.E. and R.D.S. would like to thank J. A. le Roux and C. Schreiner for many useful discussions.

ORCID iDs

N. Eugene Engelbrecht https://orcid.org/0000-0003-3659-7956

References

Adhikari, L., Zank, G. P., Hunana, P., et al. 2017, ApJ, 841, 85
Aggarwal, P., Taylor, D. K., Smith, C. W., et al. 2016, ApJ, 822, 94
Alexandrova, O., Carbone, V., Veltri, P., & Sorriso-Valvo, L. 2008, ApJ, 674, 1153
Alexandrova, O., Saur, J., Lacombe, C., et al. 2009, PhRvL, 103, 165003
Batchelor, G. K. 1970, The Theory of Homogeneous Turbulence (Cambridge: Cambridge Univ. Press)
Bavassono, B., Pietropaolo, E., & Bruno, R. 1998, JGR, 103, 6521
Bavassono, B., Pietropaolo, E., & Bruno, R. 2000a, JGR, 105, 15959
Bavassono, B., Pietropaolo, E., & Bruno, R. 2000b, JGR, 105, 12697
Bieber, J. W., Matthaeus, W. H., Smith, C. W., et al. 1994, ApJ, 420, 294
Bourouaine, S., Alexandrova, O., Marsch, E., & Maksimovic, M. 2012, ApJ, 749, 102
Breech, B., Matthaeus, W. H., Minnie, J., et al. 2005, GeoRL, 32, 6103
Breech, B. A., Matthaeus, W. H., Cranmer, S. R., Kasper, J. C., & Oughton, S. 2009, JGR, 113, 8105
Breech, B. A., Matthaeus, W. H., Minnie, J., et al. 2008, JGR, 113, 8105
Bruno, R., & Carbone, V. 2013, LRSP, 10, 2
Cannon, B. E., Smith, C. W., Isenberg, P. A., et al. 2014, ApJ, 787, 133
Chashei, I. V., & Fahr, H. J. 2014a, SoPh, 289, 1359
Chashei, I. V., & Fahr, H. J. 2014b, A&A, 571, A78
Coleman, P. J. 1968, ApJ, 153, 371
Cranmer, S. R., Matthaeus, W. H., Breech, B. A., & Kasper, J. C. 2009, ApJ, 702, 1604
Cranmer, S. R., & van Ballegooijen, A. A. 2012, ApJ, 754, 92
Dröge, W. 2000, SSRv, 93, 121
Dröge, W., Achatz, U., Wanner, W., Schlickeiser, R., & Weibberenz, G. 1993, ApJL, 407, L95
Engelbrecht, N. E., & Burger, R. A. 2010, AdSpR, 45, 1015
Engelbrecht, N. E., & Burger, R. A. 2013a, ApJ, 772, 46
Engelbrecht, N. E., & Burger, R. A. 2013b, ApJ, 779, 158
Engelbrecht, N. E., & Burger, R. A. 2015, ApJ, 814, 152
Engelbrecht, N. E., & Strauss, R. D. 2015, A&A, 579, A120
Ferreira, S. E. S., Potgieter, M. S., Burger, R. A., et al. 2001a, JGR, 106, 29313
Ferreira, S. E. S., Potgieter, M. S., Burger, R. A., Heber, B., & Fichtner, H. 2001b, JGR, 106, 24979
Gary, S. P., & Nishimura, K. 2004, JGR, 109, A02109
Hamilton, K., Smith, C. W., Vasquez, B. J., et al. 2008, JGR, 113, A01106
Hellinger, P., & Trávníček, P. M. 2016, ApJ, 832, 32
Howes, G. G. 2010, MNRAS, 409, L104
Howes, G. G. 2011, ApJ, 738, 40
Hunana, P., & Zank, G. P. 2010, ApJ, 718, 148
Isenberg, P. A. 2005, ApJ, 623, 502
Isenberg, P. A., Smith, C. W., Matthaeus, W. H., & Richardson, J. D. 2010, ApJ, 719, 716
Jokipii, J. R. 1966, ApJ, 146, 480
Leamon, R. J., Matthaeus, W. H., Smith, C. W., & Wong, H. K. 1998a, ApJ, 507, L181
Leamon, R. J., Matthaeus, W. H., Smith, C. W., Zank, G. P., & Mullan, D. J. 2000, ApJ, 537, 1054
Leamon, R. J., Smith, C. W., Ness, N. F., & Matthaeus, W. H. 1998b, JGR, 103, 4775
Marsch, E., Muhlhauser, K.-H., Schwenn, R., et al. 1982, JGR, 87, 52
Marsch, E. 2006, LRSP, 3, 1
Matthaeus, W. H., Dasso, S., Weygand, J. M., et al. 2005, PhRvL, 95, 231101
Matthaeus, W. H., Parashar, T. N., Wan, M., & Wu, p. 2016, ApJL, 827, L7
Matthaeus, W. H., Zank, G. P., Smith, C. W., & Oughton, S. 1999, PhRvL, 82, 3444
McComas, D. J., Barraclough, B. L., Funsten, H. O., et al. 2000, JGR, 105, 10419
Meyer-Vernet, N., & Issautier, K. 1998, JGR, 103, 29705
Newbury, J. A., Russell, C. T., Phillips, J. L., & Gary, S. P. 1998, JGR, 103, 9553
Ng, C. S., Bhattacharjee, A., Munsi, D., Isenberg, P. A., & Smith, C. W. 1998, JGR, 115, A02101
Oughton, S., Matthaeus, W. H., & Dmitruk, P. 2006, PhPl, 13, 042306
Oughton, S., Matthaeus, W. H., Smith, C. W., Bieber, J. W., & Isenberg, P. A. 2011, JGR, 116, 8105
Oughton, S., Matthaeus, W. H., Wan, M., & Osman, K. T. 2015, Phil. Trans.R. Soc. A, 373, 20140152
Parashar, T. N., Salem, C., Wicks, R. T., et al. 2015, JPlPh, 81, 905810513
Parker, E. N. 1958, ApJ, 128, 664
Pei, C., Bieber, J. W., Breech, B., et al. 2010, JGR, 115, 3103
Perri, S., & Balogh, A. 2010, GeoRL, 37, 17102
Phillips, J. L., Feldman, W. C., Gosling, J. T., & Scime, E. E. 1995, AdSpR, 16, 95
Pilipp, W. G., Miggenrieder, H., Muhlhauser, K.-H., Rosenbauer, H., & Schwenn, R. 1990, JGR, 95, 6305
Richardson, J. D., Paularena, K. I., Lazarus, A. J., & Belcher, J. W. 1995, GeoRL, 22, 325
Roberts, D. A., Goldstein, M. L., Klein, L. W., & Matthaeus, W. H. 1987a, JGR, 92, 12023
Roberts, D. A., Klein, L. W., Goldstein, M. L., & Matthaeus, W. H. 1987b, JGR, 92, 11021
Roberts, O. W., & Li, X. 2015, ApJ, 802, 1
Sahraoui, F., Goldstein, M. L., Robert, P., et al. 2009, PhRvL, 102, 231102
Schlickeiser, R. 2002, Cosmic Ray Astrophysics (Germany: Springer)
Schreiner, C., Kilian, P., & Spanier, F. 2017, CoPhC, 21, 947
Scime, E. E., Badeau, A. E., Jr., & Littleton, J. E. 1999, GeoRL, 26, 2129
Scime, E. E., Bame, S. J., Feldman, W. C., et al. 1994, JGR, 99, 23401
Scudder, J. D. 2015, ApJ, 809, 126
Shalchi, A. 2009, Nonlinear Cosmic Ray Diffusion Theories (Germany: Springer)
Sittler, E. C., & Scudder, J. D. 1980, JGR, 85, 5131
Smith, C. W., Hamilton, K., Vasquez, B. J., & Leamon, R. J. 2006b, ApJ, 645, L85
Smith, C. W., Isenberg, P. A., Matthaeus, W. H., & Richardson, J. D. 2006a, ApJ, 638, 508
Smith, C. W., Vasquez, B. J., & Hollweg, J. V. 2012, ApJ, 745, 8
Smith, W. S., Matthaeus, W. H., Zank, G. P., et al. 2001, JGR, 106, 8253
Steinacker, J., & Miller, J. A. 1992, ApJ, 393, 764
Stix, T. H. 1962, The Theory of Plasma Waves (New York: McGraw-Hill)
Strauss, R. D., Dresing, N., & Engelbrecht, N. E. 2017, ApJ, 837, 43
Strauss, R. D., Potgieter, M. S., Büsching, I., & Kopp, A. 2011, ApJ, 735, 83
Štverák, Š, Trávníček, P. M., & Hellinger, P. 2015, JGR, 120, 8177
Tan, L. C., Reames, D. V., Ng, C. K., Shao, X., & Wang, L. 2011, ApJ, 728, 133

Teufel, A., & Schlickeiser, R. 2003, A&A, 397, 15
Vainio, R. 2000, ApJS, 131, 519
Weygand, J. M., Matthaeus, W. H., Dasso, S., et al. 2009, JGR, 114, 7213
Weygand, J. M., Matthaeus, W. H., Dasso, S., & Kivelson, M. G. 2011, JGRA, 116, A08102
Wiengarten, T., Oughton, S., Engelbrecht, N. E., et al. 2016, ApJ, 833, 17
Zank, G. P. 1999, SSRv, 89, 413
Zank, G. P., Adhikari, L., Hunana, P., et al. 2017, ApJ, 835, 147
Zank, G. P., Dosch, A., Hunana, P., et al. 2012, ApJ, 745, 35
Zank, G. P., Matthaeus, W. H., & Smith, C. W. 1996, JGR, 101, 17093